

JGR Space Physics

RESEARCH ARTICLE

10.1029/2020JA028090

Key Points:

- Chorus rising tone elements/packets are found to be monochromatic
- The largest amplitude waves within a subelement have constant frequency
- The ends of the packets have the greatest frequency deviations; increases and decreases are detected at both ends

Correspondence to:

B. T. Tsurutani,
bruce.tsurutani@gmail.com

Citation:

Tsurutani, B. T., Chen, R., Gao, X., Lu, Q., Pickett, J. S., Lakhina, G. S., et al. (2020). Lower-band “monochromatic” chorus riser subelement/wave packet observations. *Journal of Geophysical Research: Space Physics*, 125, e2020JA028090. <https://doi.org/10.1029/2020JA028090>

Received 7 APR 2020

Accepted 28 AUG 2020

Accepted article online 22 SEP 2020

Lower-Band “Monochromatic” Chorus Riser Subelement/Wave Packet Observations

Bruce T. Tsurutani¹ , Rui Chen^{2,3} , Xinliang Gao^{2,3} , Quanming Lu^{2,3} , Jolene S. Pickett⁴ , Gurbax S. Lakhina⁵ , Abhijit Sen⁶, Rajkumar Hajra⁷ , Sang A Park⁸, and Barbara J. Falkowski⁹

¹Jet Propulsion Laboratory, California Institute of Technology, Pasadena, CA, USA, ²CAS Key Laboratory of Geospace Environment, Department of Geophysics and Planetary Science, University of Science and Technology of China, Hefei, China, ³CAS Center for Excellence in Comparative Planetology, Hefei, China, ⁴Department of Physics and Astronomy, University of Iowa, Iowa City, IA, USA, ⁵Indian Institute of Geomagnetism, Navi Mumbai, India, ⁶Institute for Plasma Research, Gandhinagar, India, ⁷Indian Institute for Technology Indore, Indore, India, ⁸Electrical Engineering and Computer Sciences, University of California, Berkeley, CA, USA, ⁹Physics and Astronomy Departments, Glendale Community College, Glendale, CA, USA

Abstract Three lower-band ($f < 0.5$ fce) chorus riser elements detected in the dayside generation region were studied in detail using the Van Allen Probe data. Two subelements/wave packets within each riser were examined for their wave “frequency” constancy within seven consecutive wave cycles. The seven wave cycles contained the maximum amplitudes of the subelements/packets. Maximum variance B1 zero crossings were used for the identification of wave cycle start and stop times. It is found that the frequency is constant to within $\sim 3\%$ (one standard deviation), with no evidence of upward frequency sweeping over the seven cycles. Continuous wavelet power spectra for the duration of the seven cycles confirm this conclusion. The implication is that a chorus riser element is composed of coherent approximately “monochromatic” steps instead of a gradual sweep in frequency over the whole element. There was no upward frequency stepping where the wave amplitude was the largest, contrary to the sideband theory prediction. It is shown that a chorus riser involves instability of cyclotron resonant energetic electrons from ~ 6 to ~ 40 keV at $L = 5.8$, that is, essentially the whole substorm electron energy spectrum. The above findings may have important consequences for possible wave generation mechanisms. Some new ideas for mechanisms are suggested in conclusion.

1. Introduction

An electromagnetic whistler mode plasma wave was named “chorus” because when it was initially detected on the ground, it sounded like a “chorus” of birds chirping (Isted & Millington, 1957; Storey, 1953). This name remains in use today. Chorus is generated in the Earth’s outer zone ($5 < L < 10$) low-plasma β ($<<1$) portion of the magnetosphere, at and near the magnetic equator (Lauben et al., 2002; LeDocq et al., 1998; Li, Bortnik, et al., 2011; Meredith et al., 2001, 2003; Tsurutani & Smith, 1974, 1977) associated with the electron loss cone/temperature anisotropy plasma instability (Kennel & Petschek, 1966). In the above, L corresponds to a dipole magnetic field line that crosses the Earth’s magnetic equator at an Earth radii ($Re = 6,378$ km) distance equal to the L value. Plasma β is defined as the plasma thermal pressure divided by the magnetic pressure. The chorus plasma waves can propagate through the magnetosphere to the ionosphere and to ground (Helliwell, 1965).

The overall scenario for the generation of these waves is thus southward interplanetary magnetic fields (IMFs) lead to reconnection with the Earth’s dayside magnetopause fields and resultant nightside reconnection of magnetotail magnetic fields (Dungey, 1961) creates substorms (Akasofu, 1964; Tsurutani & Meng, 1972). This reconnection process is the prime mechanism of solar wind energy transfer to the Earth’s magnetosphere (Tsurutani et al., 2006, 2020). The magnetotail reconnection during substorms leads to the energization of ~ 100 eV to 1 keV plasma sheet plasma to energies of ~ 10 to 100 keV (DeForest & McIlwain, 1971) by compression, as the inner edge of the plasma sheet is injected into the nightside magnetosphere to distances as close as $L = 4$ (Soraas et al., 2004). The plasma injection conserves the particles’ first two adiabatic invariants which leads to a temperature anisotropy of both energetic electrons and protons. The $T_{\perp}/T_{\parallel} > 1$ anisotropy of the ~ 10 to 100 keV electrons causes the loss cone/temperature anisotropy

instability and the generation of the chorus waves as the electrons gradient and curvature drift from the midnight sector through dawn to local noon (Li, Bortnik, et al., 2011; Meredith et al., 2001, 2003; Tsurutani & Smith, 1977; Tsurutani et al., 1979). In the above T_{\perp} and T_{\parallel} are the electron temperatures perpendicular and parallel to the ambient magnetic field, respectively.

There are similar magnetohydrodynamic (MHD) wave modes (McGuire et al., 1983; Nave et al., 1991) and “beam modes” (Heidbrink, 1995) named “chirps” detected in plasma devices. More recently, electromagnetic whistler mode “chirping” has been studied as well (Compernolle et al., 2015). As the name implies, these short duration bursts seem similar to chorus. Although it is suspected that the general mechanism might be the same for chirps and magnetospheric chorus, the exact relationship is still not well understood (Compernolle et al., 2015). In this paper, we will focus only on magnetospheric chorus waves.

For magnetospheric chorus, the wave “chirping” has to do with each ~0.1 to 1.0 s chorus “element” or “chirp” starting at an onset frequency and then rising to a higher frequency within a fraction of a second (see examples of chorus elements in Goldstein & Tsurutani, 1984; Helliwell, 1965; Tsurutani et al., 2009, 2013). It was shown by Santolik et al. (2003, 2004) that each element is composed of a number of “subelements” or “packets.” Tsurutani et al. (2009) showed that each chorus subelement was coherent when examined in the chorus generation region close to the magnetic equator. Later, Tsurutani et al. (2011) showed that chorus becomes incoherent as the waves propagate further away from the magnetic equator.

The level of wave coherency is of interest not only in an abstract theoretical sense. It was shown by Bellan (2013), Lakhina et al. (2010), Mourenas et al. (2018), and Yoon and Bellan (2020) that wave-particle interactions involving coherent whistler mode waves will diffuse particle pitch angles at a considerably higher rate than predicted by the incoherent waves assumed by Kennel and Petschek (1966). Tsurutani et al. (2013) have argued that auroral zone bremsstrahlung consisting of ~0.1 to 1.0 s “microbursts” (Anderson & Milton, 1964) can only be accounted for by pitch angle scattering of energetic electrons with coherent or quasi-coherent cyclotron resonant waves.

The question of what the microstructure of chorus subelements looks like has arisen. This could help determine if the underlying assumptions in existing theories of the frequency increases in the chorus risers are correct or not. As one example, chorus riser elements have been nicely modeled by Demekhov et al. (2017), Lu et al. (2019), and Omura et al. (2008). The amplitude of the waves increases when they leave the equatorial generation region and propagate toward higher magnetic latitudes in a dipole magnetic field where the local cyclotron frequency is higher. The frequency sweep of a chorus element occurs as a result of nonlinear wave growth due to the formation of an electromagnetic electron hole in phase space by wave trapping of resonant electrons. This mechanism will predict a smooth and gradual increase in chorus element frequency with time. It however does not address the issue of the occurrence of subelements within the chorus risers.

Another prominent chorus generation theory is that of sideband formation (Nunn, 1986; Trakhengerts et al., 2004). For the latter mechanism, wave upward stepping occurs with strong wave amplitudes at about the trapping frequency of the resonant electrons. Both of these two general mechanisms can be tested by a detailed examination of chorus subelements.

The purpose of this paper is to examine isolated lower-band ($f < 0.5$ fce) intense chorus riser elements from the Van Allen Probe data. In the above, f is the wave frequency and fce is the electron cyclotron frequency. In particular, we will be asking the question of how the chorus riser increases in frequency. Does the frequency increase slowly across each and every subelement within the element? Or does it increase just at the beginnings and ends of the subelements? Is there any evidence that the wave frequency increases with higher amplitude chorus waves, as implied by sideband theory? We will use a new and simple technique to attempt to answer the above questions. The implication of the results will be discussed in detail.

2. Method of Data Analyses

Triaxial search coil magnetic field measurements of outer zone chorus were made by the Van Allen Probes satellite A. Specifically, the measurements were obtained from the Electric and Magnetic Field Instrument Suite and Integrated Science (EMFISIS) wave instrument (Kletzing et al., 2013). In this study the burst waveform data with a sampling rate of 35 kHz from the Waveform Receiver (WFR) of EMFISIS were used. The triaxial fluxgate magnetometer (MAG) was used to obtain the direction and magnitude of the ambient

magnetospheric magnetic field. MAG was part of the EMFISIS instrument suite. The EMFISIS data can be obtained from the [website](https://spdf.gsfc.nasa.gov/pub/data/rbsp/).

For the analyses of the high time resolution triaxial search coil magnetometer data, we use the Sonnerup and Cahill (1967) minimum variance technique applied to the electromagnetic plasma waves (Smith & Tsurutani, 1976). The three mutually orthogonal components of the wave field are used to compute the nine elements of the zero-lag covariance matrix. This matrix is diagonalized and then the magnetic field wave components rotated into the new coordinate system. The magnetic field wave component along the maximum variance direction is called the B1 component, the one along the intermediate variance direction is called B2, and the one along the minimum variance direction is called B3. It has been shown by Verkhoglyadova et al. (2010) that the minimum variance direction of the magnetic component of whistler mode electromagnetic waves as chorus is the direction of wave propagation \mathbf{k} . However, in general this is not true for the electric component of electromagnetic waves.

A continuous wavelet transform using a Morlet mother wavelet function was applied to the magnetic components of chorus subelements. The Morlet wavelet consists of a plane wave modified by a Gaussian. It has a zero mean value, is localized in both time and frequency space, has several smooth oscillations, and its period is a well-defined quantity that approximates the period of a signal obtained through Fourier analysis. The wavelet power spectrum (the sum of the three orthogonal components) has a time resolution of 2.9×10^{-5} s. It should be noted that the intensity legend in the various wavelet power spectra that are displayed in the paper varies from one spectrum to the next. Each spectrum was adjusted separately so that the frequency with maximum power (shown in dark red) would be visible and noticeable to the reader.

Three intervals of chorus riser elements were selected for this study. We selected chorus intervals using four criteria. Criterion (1), the waves were detected within $\pm 10^\circ$ of the magnetic equator ($MLAT \leq |10^\circ|$) or the wave generation region (Lauben et al., 2002; LeDocq et al., 1998; Taubenschuss et al., 2016). Criterion (2) is that the waves are detected within the local time of approximately dawn to midmorning ($\sim 06 \leq MLT \leq 09$), where MLT is the magnetic local time. This criterion was chosen because chorus is most intense in the post dawn sector, but at greater MLT the distribution of intense chorus extends to higher absolute magnetic latitudes ($|MLAT|$) (Li, Bortnik, et al., 2011; Meredith et al., 2001, 2003; Tsurutani & Smith, 1977). There are two possibilities for this latter observation. One is that the wave generation region is extended to high $|MLAT|$ values due to the flattening of the ambient dayside magnetic fields by the solar wind. However, another possible explanation is that chorus is also being generated within high-latitude minimum B pockets with consequential wave propagation down toward the magnetic equator (Tsurutani et al., 2009). Because of the latter possibility of wave source region contamination, we have excluded chorus detected in the $\sim 10 \leq MLT \leq 14$ region for this study. Criterion (3) is that the waves are detected far from the magnetopause location of 10 to 13 Re, where the wave amplitudes are relatively weak (Li, Bortnik, et al., 2011). Criterion (4) is that the chorus risers be in the lower-band chorus frequency range ($f \leq 0.5$ fce: Tsurutani & Smith, 1974). It has been shown that upper band chorus is not only statistically weaker in amplitude but may have a different generation mechanism (Li, Thorne, et al., 2011; Schriver et al., 2010; Taubenschuss et al., 2016). The reasons for the above four criteria were to select high-intensity dayside chorus typical of their general properties (Goldstein & Tsurutani, 1984; Li, Bortnik, et al., 2011; Meredith et al., 2003; Tsurutani & Smith, 1977).

Lower-band, rising tone dayside chorus is the most common type of emission detected and thus is the focus of this study. Falling tone or flat frequency-time chorus has been observed (Agapitov et al., 2013; Aryan et al., 2014; Breuillard et al., 2014; Li, Thorne, et al., 2011; Taubenschuss et al., 2014, 2015, 2016; Tsurutani & Smith, 1974; Tsurutani et al., 2013), but these types of chorus occur less frequently and with less intensity, so will be excluded from this study.

3. Results

3.1. Riser 1

Figure 1 shows some Van Allen Probe A chorus riser elements taken when the spacecraft was near local dawn ($MLT = 5.8$), at $L = 5.8$ and a $MLAT$ of 3.1° . Panel (a) shows the wave magnetic field intensity, and panel (b) shows the wave electric field intensity of the electromagnetic waves. The wave intensities are given by the color code legends on the right of the two panels. Panel (c) gives the wave normal angle (WNA). This

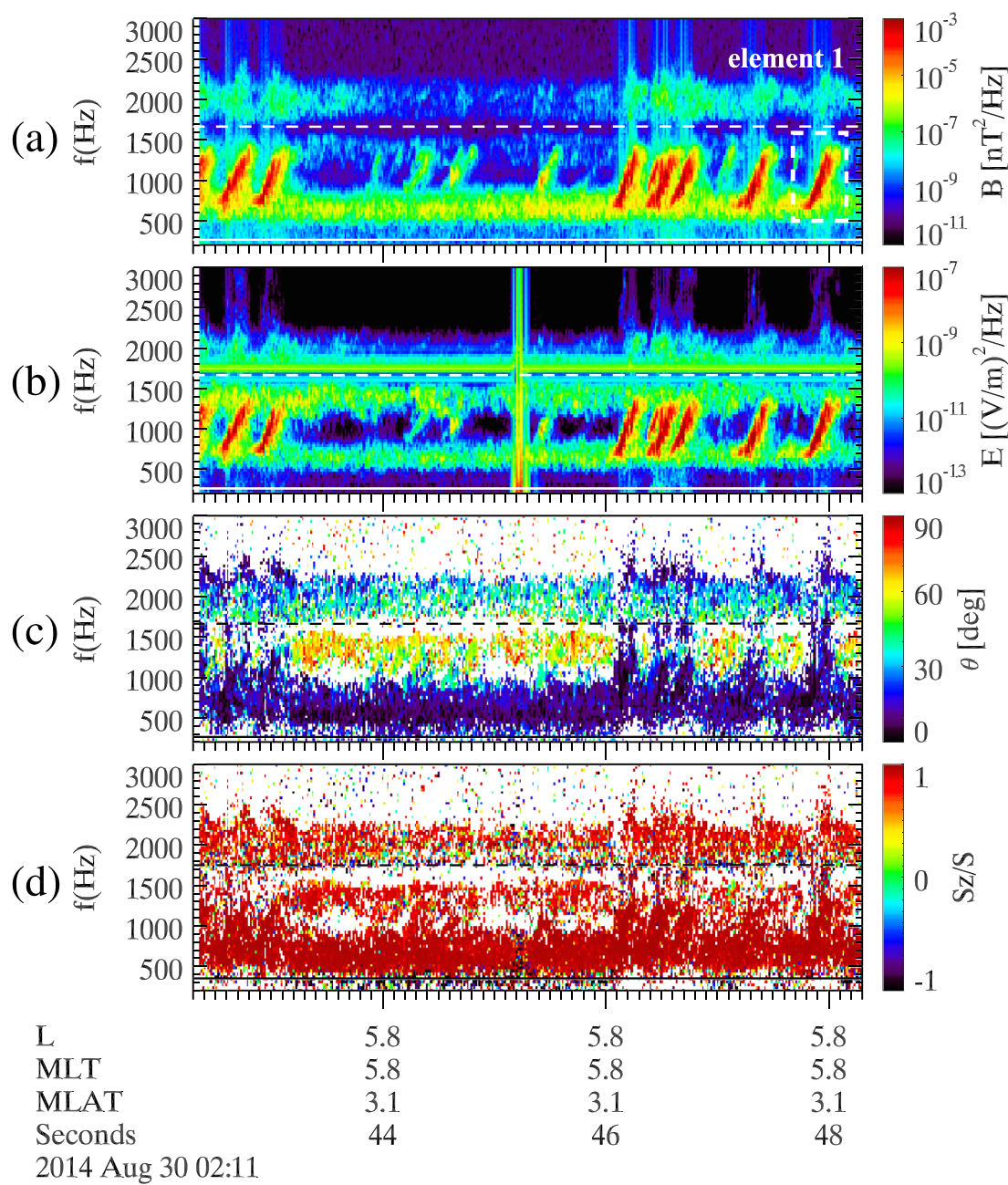


Figure 1. An interval of chorus rising tone elements taken at ~02:11 UT on 30 August 2014. This was generated from the continuous burst waveform data with high time resolution (~30 μ s). The large horizontal time tick marks are at 2 s intervals. From top to bottom are (a) the wave magnetic field intensity, (b) the wave electric field intensity, (c) the wave normal angle relative to the ambient dc magnetic field \mathbf{B}_0 , and (d) the ratio S/S_z . S is the Poynting Flux intensity and S_z is its component along \mathbf{B}_0 . The local value of 0.1 fce is shown by a horizontal solid line, and 0.5 fce is indicated by a horizontal dashed line. The latter two values are indicated in all four panels and are reiterated for reference.

is the angle between the wave vector \mathbf{k} and the ambient magnetic field, \mathbf{B}_0 . Panel (d) shows a slightly different parameter than given in panel (c). It is the ratio S/S_z where S is the Poynting Flux and S_z is the component along \mathbf{B}_0 .

The top two panels of the figure show a number of chorus rising elements. The risers all have a similar shape. They start out of a hiss-like band near $f \sim 600$ Hz and rise to $f \sim 1300$ Hz. The risers lie between $f = \sim 0.2$ and ~ 0.4 fce. The risers are lower-band chorus ($f \leq 0.5$ fce). These elements rise with a near-linear frequency-time

profile. The time durations of the events are typical of chorus, ~0.2 s for each element. Some of the risers at the beginning of the interval near ~2011:42 UT and also near ~2011:46 UT overlap with each other. The overlap time is as close as ~0.1 to 0.2 s. An isolated riser element occurs near the end of the interval displayed. This latter event was selected for detailed analysis. This chorus element is indicated by a white dashed box around the element in the top panel (a).

The third panel indicates that the wave vector \mathbf{k} is directed fairly along the magnetic field direction $\mathbf{B_0}$. This is indicated by the blue coloring at times when chorus risers are present. The fourth panel indicates that S/S_z is close to unity by the red coloration at times when chorus risers are present.

It is useful to briefly examine what electron energies are involved in the generation of the chorus elements. The wave-particle cyclotron resonance condition for the nonrelativistic case is given by:

$$f - k_{\parallel} V_{\parallel} / 2\pi = n f_{ce} \quad (1)$$

where f is the wave frequency, k_{\parallel} is the wave \mathbf{k} component along the ambient magnetic field direction $\mathbf{B_0}$, V_{\parallel} is the particle velocity parallel to the magnetic field, and n is the harmonic number ($0, \pm 1, \pm 2, \dots$). For positive values of n , Equation 1 represents the normal cyclotron resonant condition where the waves and particles are traveling in opposite directions to each other. The waves will be Doppler shifted up to the electron cyclotron frequency or its harmonics. The less energetic the electrons, the higher the frequency of the waves needed for resonance.

For the fundamental normal electron cyclotron resonance ($n = 1$) and wave parallel propagation, the expression in 1 can be divided by $k = k_{\parallel}$ and thus be written as follows:

$$V = V_{ph} (1 - f_{ce}/f) \quad (2)$$

Here $V_{ph} = 2\pi f/k$ is the parallel wave phase speed. The resonant parallel kinetic energy is thus given by:

$$E = m V_{ph}^2 (1 - f_{ce}/f)^2 / 2 \quad (3)$$

If one assumes that the wave phase speed V_{ph} is $c/10$, where c is the speed of light, for cyclotron resonance the parallel kinetic energy of resonant electrons for the ~600 Hz (~0.2 fce) lower frequency end of the chorus riser element will be $E \sim 40$ keV at $L = 5.8$. For the higher-frequency end of the chorus riser element of $f \sim 1300$ Hz (~0.4 fce), the resonant kinetic energy of the electrons will be $E \sim 6$ keV.

It is generally assumed that the energy range of substorm-injected electrons is ~10 to 100 keV. If one slightly lowered the estimated wave phase velocity V_{ph} to $\sim c/7$, then the ~10 to 100 keV energy range would be matched almost perfectly. Unfortunately, it is not possible to measure the thermal plasma densities accurately at such low values, and our calculation cannot be done with greater uncertainty. However, it can be said that the results of the above back-of-the-envelope calculation indicate that essentially the whole energy range of the substorm magnetospheric electrons is involved in a single riser element. On the other hand, the rough estimate of the energy range of ~6 to 40 keV for resonant electrons with the chorus element is intriguing. Since the electron spectrum has a power law dependence, there are far fewer particles at higher energies than at lower energies. Thus, the loss cone/temperature anisotropy instability of electrons with energies of ~40 to 100 keV may not be involved with chorus element generation. This speculation can be tested using in situ measurements of waves and particles on a spacecraft like the Van Allen Probes. However, this task is beyond the scope of the present paper.

A detailed view of a large portion of the chorus riser selected in Figure 1 is shown in Figure 2. The top panel indicates the presence of five subelements within the riser element. Each subelement has the form of a wave packet with the packet starting with a small amplitude, growing with time to a large amplitude and then decreasing to a negligible amplitude. In between the packets/subelements there is only a very small wave amplitude present. At time 0.930 s, the wave amplitude is <0.1 nT.

The similarity in amplitudes of the minimum variance B_1 and B_2 components indicates that these subelements are circularly polarized waves. Two subelements, the second and fourth, are highlighted by red boxes in the B_1 panel. These are marked "Subelement 1" and "Subelement 2" and will be studied later.

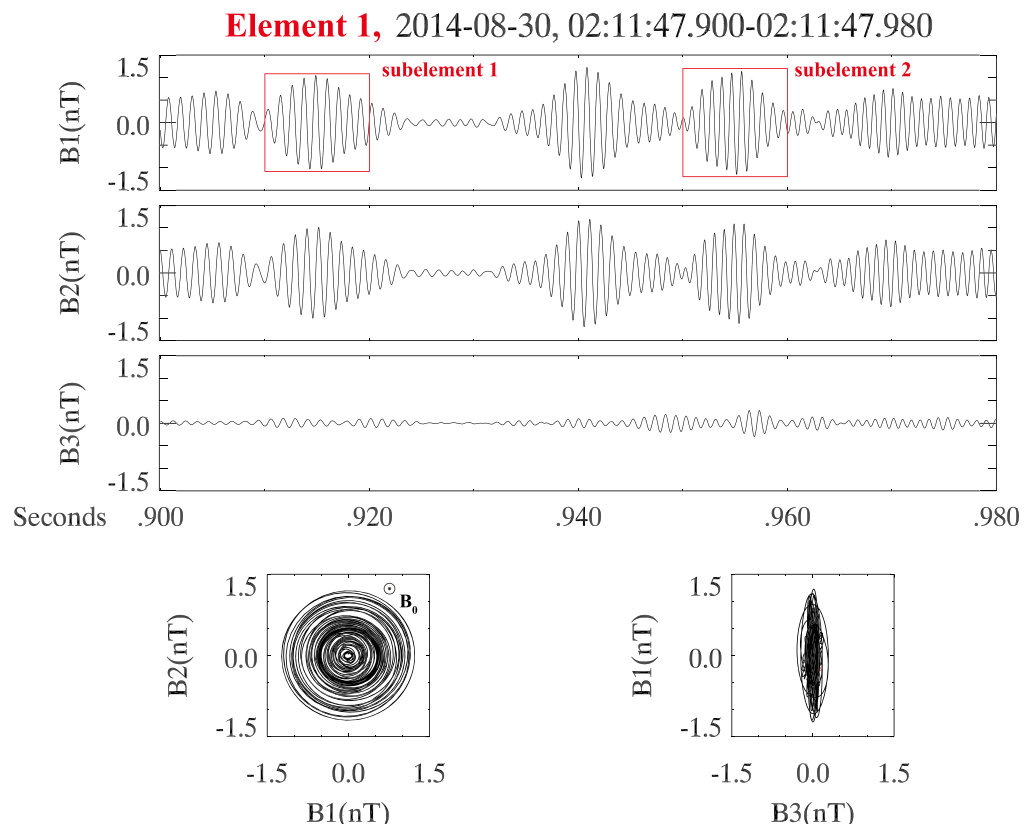


Figure 2. An ~0.08 s portion of the selected chorus riser (Riser 1) identified by the white dashed box in Figure 1. The top panel gives the three orthogonal wave magnetic field components in minimum variance coordinates B_1 , B_2 , and B_3 , respectively. The bottom left panel shows the B_1 - B_2 hodogram and the bottom right panel the B_1 - B_3 hodogram.

The B_1 - B_2 hodogram on the bottom left illustrates the circular polarization of the waves. The ambient magnetic field direction \mathbf{B}_0 is out-of-the-plane (indicated by the tip of the arrow in the panel) indicating that the waves are right-hand polarized or waves propagating in the whistler mode. The average angle of wave propagation to the magnetic field \mathbf{B}_0 is ~4°.

The B_1 - B_3 hodogram on the bottom right is shown to illustrate that the waves are planar.

Subelement 1 from Figure 2 is shown in high time resolution in Figure 3. The minimum variance analysis was done separately for this interval. The average angle of \mathbf{k} relative to the ambient magnetic field \mathbf{B}_0 is ~1.1°. The top panel shows the B_1 , B_2 , and B_3 wave components, and the bottom panel gives the B_1 - B_2 and B_1 - B_3 hodograms. The start of the interval is indicated by a red arrow in both hodograms. The waves are right-hand circularly polarized and planar.

We use the B_1 component zero crossings to identify the start and stop times of the wave cycles. The zero value of B_1 is indicated by a dashed horizontal red line. The zero crossings of B_1 are indicated by vertical dashed blue lines. Other parts of the wave phase could be used, but this method is simple and easy to visualize.

The time interval between the top times of seven wave cycles has been measured and then converted into a “frequency” value. These frequency values are given at the top of the B_1 panel. The first frequency is 849.2 Hz, and the last is 967.3 Hz. This might suggest an upward trend in frequency from the beginning to the end, but it should be noted that Cycles 3 and 4 are constant at ~893 Hz and Cycles 5 and 6 are constant at 916.2 Hz. These latter wave cycles occur when the wave amplitudes in the subelement are largest, between ~±0.8 and ±1.1 nT. The last cycle with frequency at 967.3 Hz occurs as the wave amplitude decreases to ~±0.6 nT.

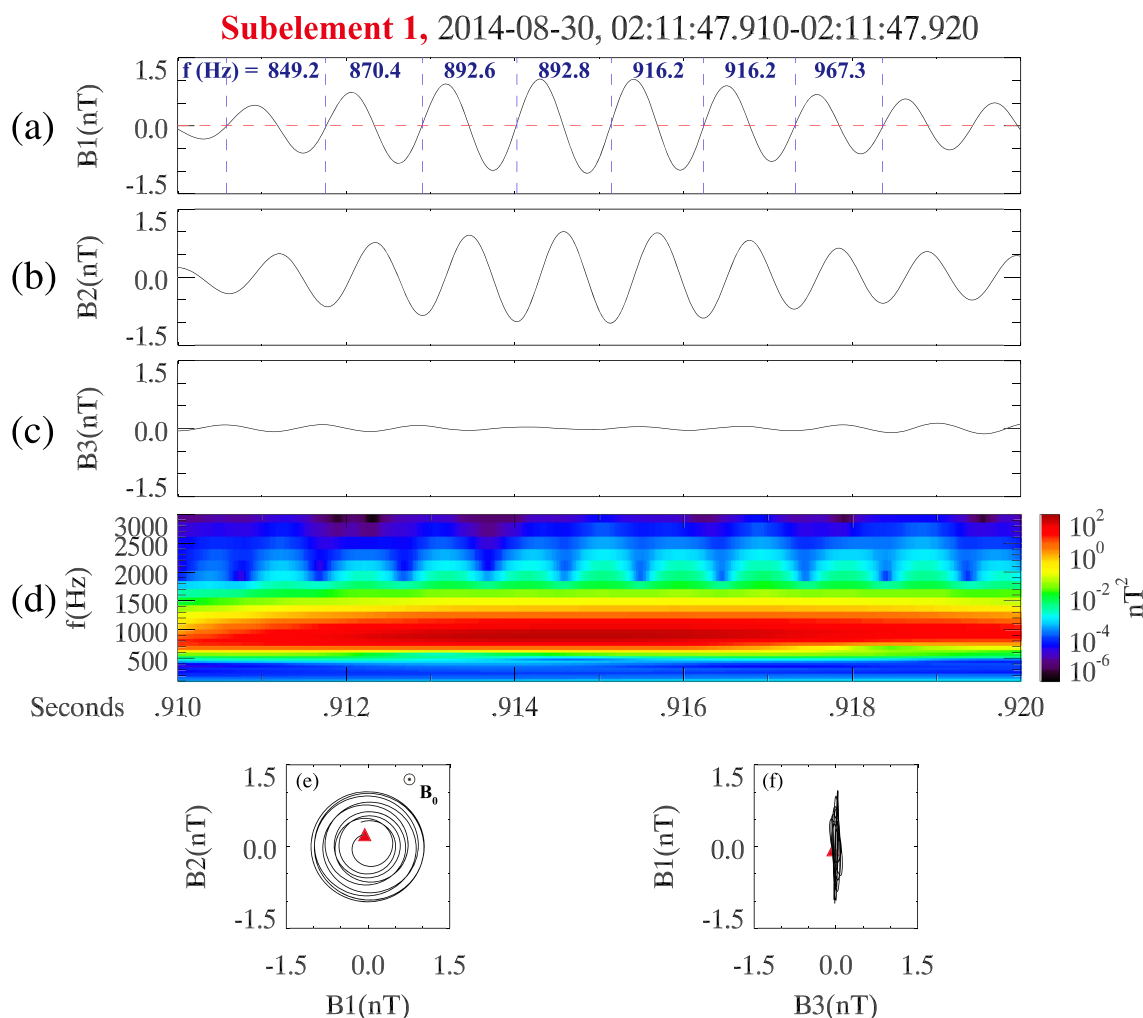


Figure 3. (a–c) Subelement 1 in high time resolution. The general format is the same as in Figure 2. Panel (d) shows the continuous wavelet power spectrum.

The mean frequency for the seven cycles is 900.7 Hz with a standard deviation of 35.1 Hz. This standard deviation is 3.9% of the mean frequency.

The continuous wavelet power spectrum given in panel (d) shows the slight rise in the frequency across the subelement. If one focusses on the darkest portion of the spectrum (dark red), this tendency can be noted. The legend for the color is given on the right of the panel. The wavelet power spectrum also indicates wave power present at frequencies both above and below the main (dark red) band. However, the power given in nT^2 for the lighter red colorations is $\sim 10^2$ to 10^3 times less intense. The dark area corresponds well to the highest intensities shown in the B_1 and B_2 waveforms in panels (a) and (b).

There are some low intensity (blue) oscillations at high frequencies near 2 kHz that the reader should ignore. These may be harmonic waves that can be noted in the FFT spectrum in Figure 1.

Figure 4 gives the details of the wave minimum variance components of Subelement 2 identified in Figure 2. The wave is right-hand circularly polarized and planar. The average \mathbf{k} is oriented at an angle $\sim 9.5^\circ$ from the ambient magnetic field direction \mathbf{B}_0 .

The zero crossings of the B_1 values are again indicated by blue vertical lines. Seven wave cycles are analyzed. Cycles 2 through 4 have relatively constant frequency of ~ 1055 Hz. These three cycles have the largest amplitudes of $\sim \pm 0.8$ to ± 1.2 nT. Cycle 5 with a decreased frequency of ~ 1024 Hz has a similar amplitude of

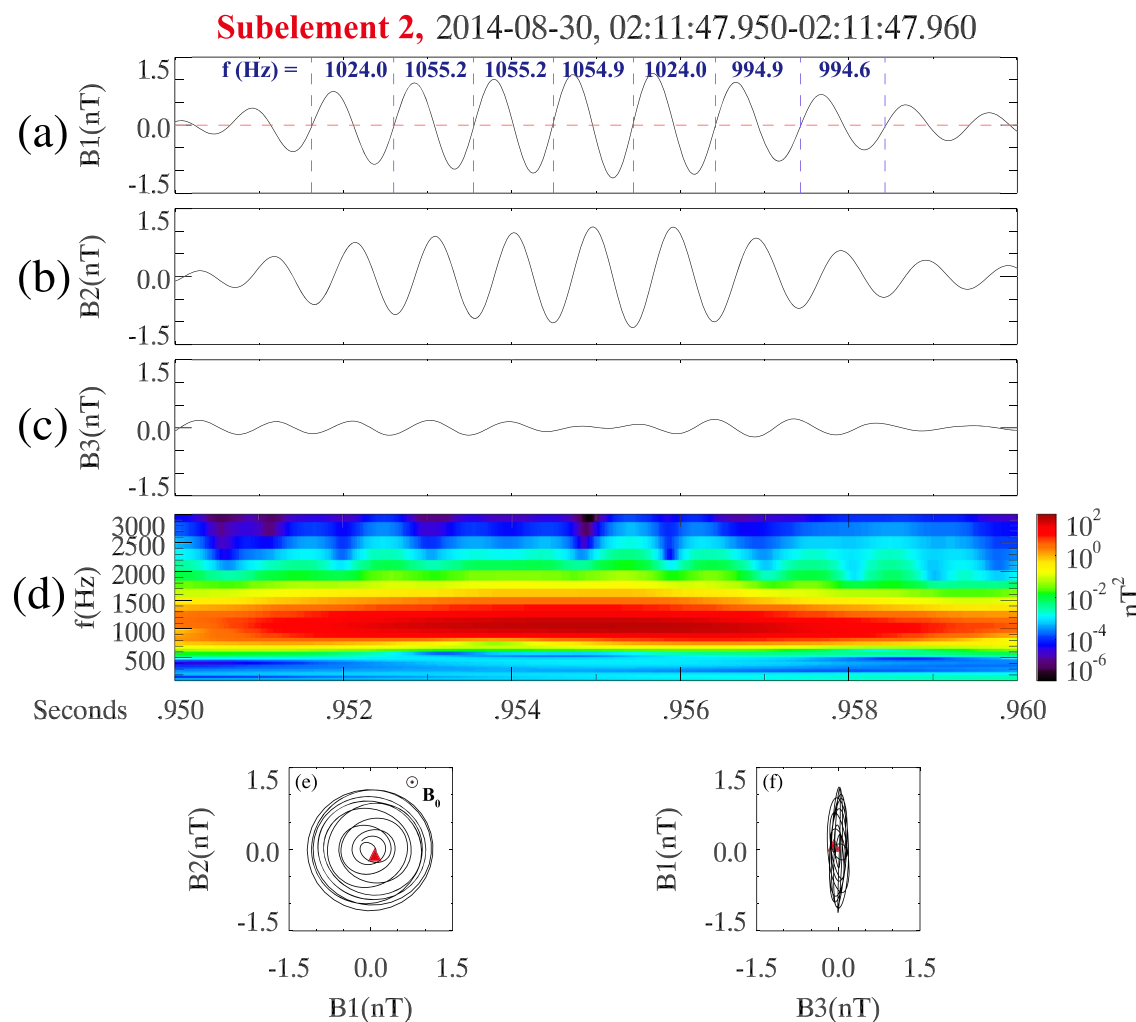


Figure 4. Subelement 2 shown in high time resolution. The format is the same as in Figure 3.

$\pm 1.1 \text{ nT}$, and Cycles 6 and 7 have lower frequencies of $\sim 994 \text{ Hz}$ as the wave amplitudes decreased to $\sim \pm 0.6$ to 0.8 nT . The ending of Subelement 2 is different from Subelement 1 where the frequency rose slightly near the end of the subelement. The ending of Subelement 2 decreased in frequency.

The mean frequency of the seven cycles of subelement 2 is 1029.0 Hz with a standard deviation of 25.2 Hz . This standard deviation is 2.4% of the mean frequency.

For the wavelet power spectrum in panel (d), the reader should again focus on the dark red portion of the plot where the wave intensities are highest. The slight decrease in frequency at the end of the subelement can be noted.

Subelement 2 occurred later in time than that of Subelement 1. Thus, since the two subelements were part of a chorus riser element, the frequency of Subelement 2 is expected to be higher than that of Subelement 1. Subelement 2 has a mean frequency of $\sim 1029.0 \text{ Hz}$ compared with $\sim 900.7 \text{ Hz}$ for Subelement 1.

3.2. Riser 2

Figure 5 gives another example of rising tone chorus detected at a MLT of 5.8 , $L = 5.7$, and $\text{MLAT} = -1.3^\circ$. These chorus rising tones have a slightly different frequency extent, frequency-time shape, and duration than the chorus elements in Figure 1. The elements extend in frequency from ~ 400 – 500 to $\sim 1900 \text{ Hz}$ or from $f \sim 0.15$ to 0.45 fce . This is again lower-band chorus. The element durations are variable, and some cases can

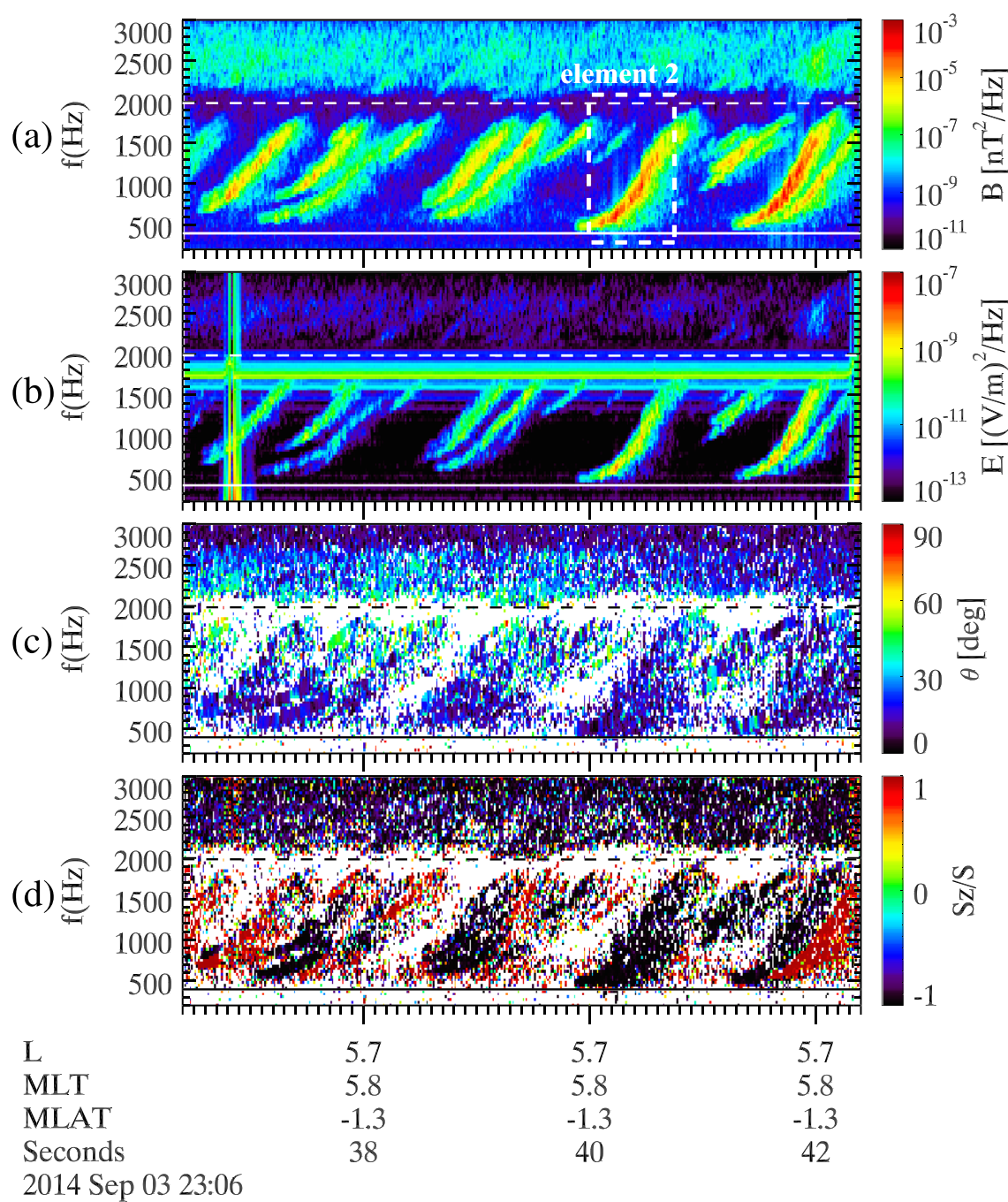


Figure 5. An interval of chorus “S-shaped” rising elements taken at ~23:06 UT on 3 September 2014. The format is the same as in Figure 1.

be as long as ~ 1.0 s. The frequency-time shape is similar to a lazy “s,” barely rising in frequency at first, then more rapidly upward and then ending with an asymptotic shape near ~ 0.5 fce. Almost all of the elements in this interval have this shape.

In the first half of the figure interval, there are multiple rising tones that are overlapping each other. The overlap time can be as short as ~ 0.1 to 0.2 s, similar to risers shown in Figure 1. The average angle of wave propagation relative to the ambient magnetic field is $\sim 17.2^\circ$. The third panel from the top shows that the waves are nearly parallel propagating relative to \mathbf{B}_0 , and the fourth panel indicates that the wave S/S_z ratio is again close to -1.0 (negative unity).

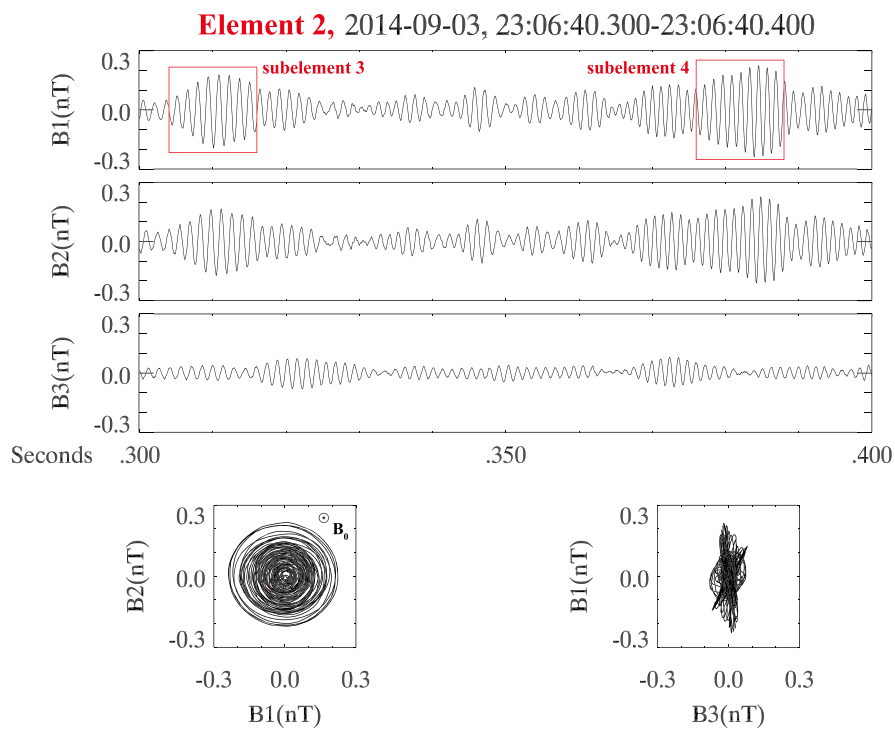


Figure 6. Element 2 shown in high resolution. The format is the same as in Figure 2. Subelements 3 and 4 are selected here for further analysis.

We have selected one isolated element for more detailed analyses. This is indicated by a dashed white box in panel (a) and is called Element 2. Note that there is a weak chorus element at high frequencies inside the box, so this riser is not totally isolated.

Figure 6 shows some of the subelements for the chorus riser/Element 2 indicated in Figure 5. The subelement shapes are similar to those in Figures 3 and 4. However, now there are two large amplitude subelements and a number of smaller amplitude, short duration subelements. The B_1 - B_2 hodogram in the bottom left panel indicates that the waves are circularly polarized. The B_1 - B_3 hodogram in the bottom right panel indicates that the wave subelements are planar, but the shift in some of the planes indicates that some of the subelements may be coming from different directions.

Figure 7 shows a high-resolution view of Subelement 3, identified in Figure 6. The wave interval had a wave \mathbf{k} direction angle of $\sim 26.7^\circ$ relative to \mathbf{B}_0 . The hodograms indicate that the waves were right-hand circularly polarized and planar.

The top panel of Figure 7 shows the “frequency” variability of the wave cycles of Subelement 3. Seven wave cycles were examined. The first cycle had $f = 725.3$ Hz with an amplitude of ± 0.10 nT. The next five cycles had the largest amplitudes, all with $B_1 > \pm 0.20$ nT. The frequency of these cycles had a narrow range from 696 to 710 Hz. In these six cycles the frequency of the first cycle was the largest and the following five cycles had smaller frequencies. The seventh cycle had a frequency of 696 Hz with a decreased amplitude of $\sim \pm 0.16$ nT. If there is a trend, it would be a decrease in frequency with time. However, it is safe to say that any trend is not strong nor obvious. The mean frequency was 704.5 Hz with a standard deviation of 10.5 Hz. This standard deviation is 1.4% of the mean frequency.

The wavelet power spectral peak power (dark red) indicates a more or less constant frequency across the entire subelement/packet (note that the intensity scale is different from that shown in Figure 3. The scale was adjusted so that the dark red peak power is distinguishable from lesser intensity frequencies). The decrease in frequency at the beginning and end of the seven cycles analyzed is difficult to see. This is, in general, consistent with the above single wave cycle analyses.

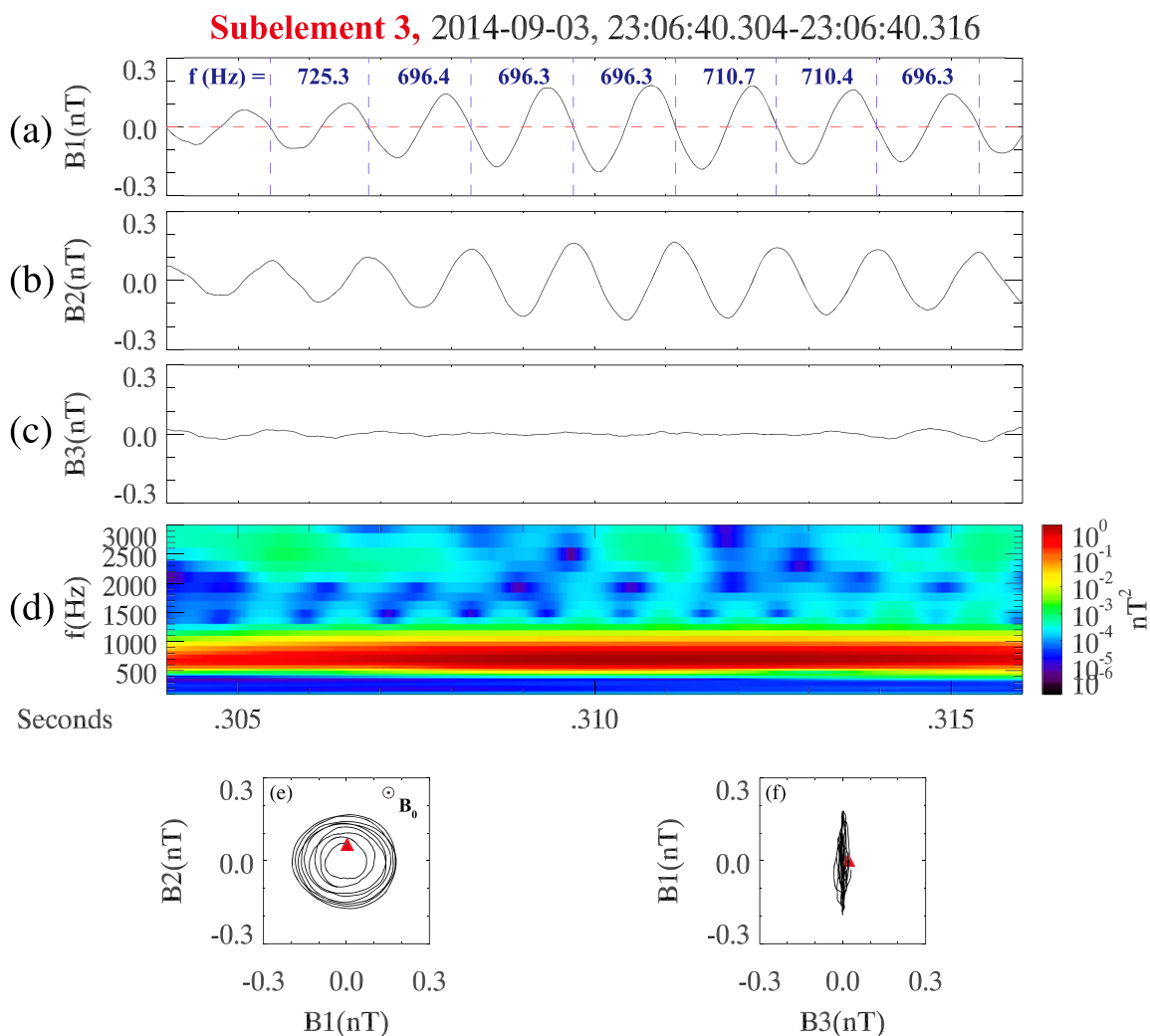


Figure 7. Detailed examination of subelement 3. The format is the same as in Figure 3.

Figure 8 shows the high-resolution plot for Subelement 4, identified in Figure 6. The waves are propagating at $\sim 17.0^\circ$ relative to the ambient magnetic field \mathbf{B}_0 and are right-hand circularly polarized and planar. This subelement is a bit unique in that it contains many cycles. We again examine seven wave cycles near where the amplitude of the waves is the largest. Since this subelement occurred later in time than Subelement 3, both of which were part of chorus riser Element 2, one expects the wave frequencies to be higher.

The first measured cycle had a frequency of 791 Hz. This was the cycle with the smallest amplitude of ± 0.16 nT. The next five wave cycles have larger amplitudes, ranging from ± 0.19 to ± 0.23 nT and have a frequency range between ~ 809 and 829 Hz. The last cycle had a slightly lower amplitude than Cycle 6, with a value of ± 0.21 nT and a higher frequency of 849 Hz. The wave packet had a frequency profile of an increase in frequency at the beginning, a flat constant frequency where the wave amplitudes peaked and an increase in frequency as the packet amplitude decreased. The wavelet power spectra frequency profile is consistent with that observed from the single cycle analyses.

Note that this subelement is at higher frequencies than that of Subelement 3 which were from ~ 696 to 710 Hz. The average frequency of the seven cycles of Subelement 4 was 818.2 Hz with a standard deviation of 17.5 Hz. This standard deviation is 2.1% of the mean frequency.

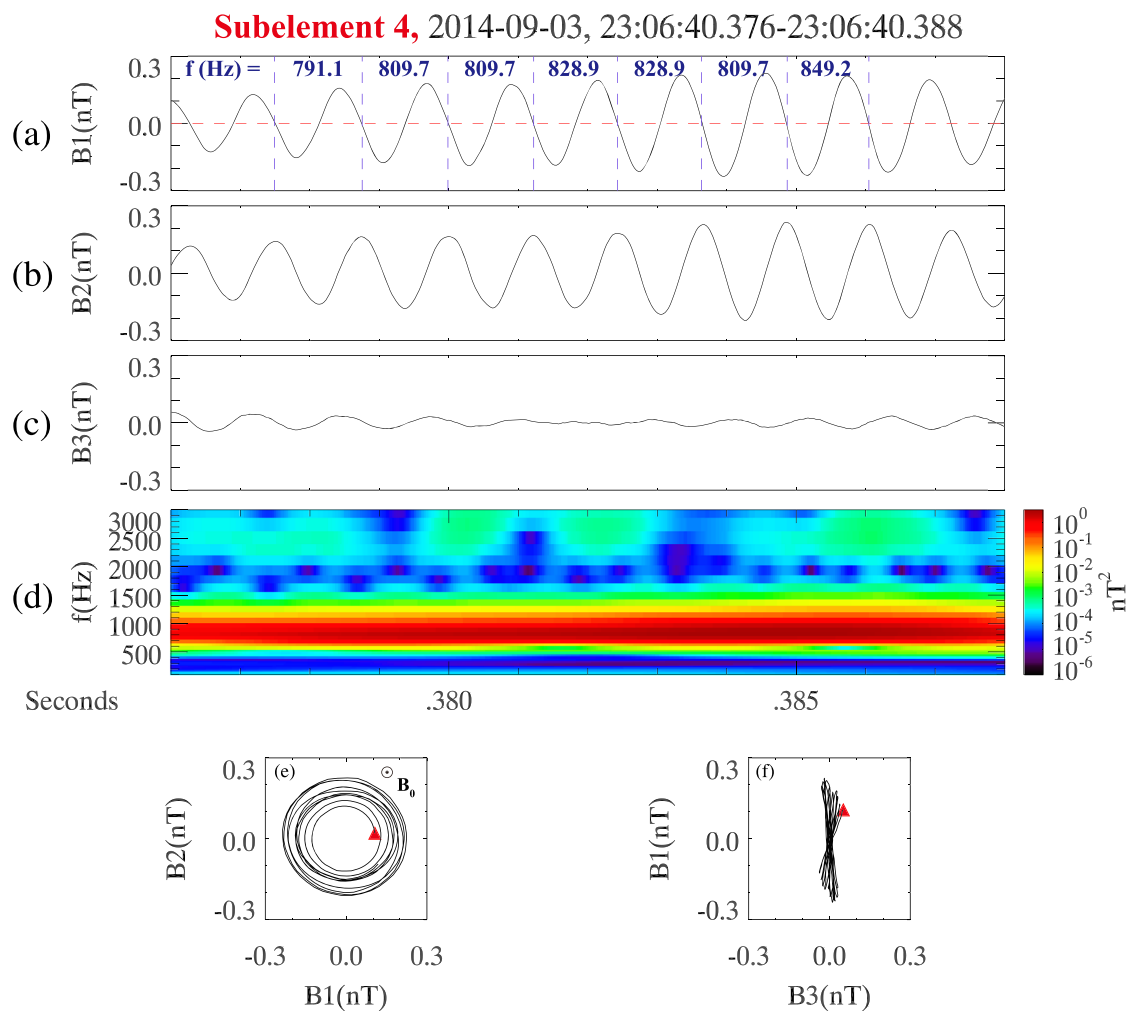


Figure 8. Subelement 4, identified in Figure 6. The format is the same as in Figure 3.

3.3. Riser 3

A third intense chorus riser element (Element 3) and two of its subelements (Subelements 5 and 6) were selected and analyzed. To save space, the figures, the description of the data, and the results of analyses have been placed in the appendix (Appendix A). This third chorus riser extended from $f = \sim 0.2$ to ~ 0.6 fce with a well-known gap at ~ 0.5 fce (Tsurutani & Smith, 1974). Only the low-frequency chorus portion was analyzed. A summary of the results of all three risers is given in Table 1.

The columns of Table 1, from left to right, are the chorus riser element number, the date and UT of the event, the MLT, L , and MLAT of the riser event. Columns 6 through 9 pertain to the subelements which are parts of

Table 1
Summary of Three Chorus Riser Elements and Two of Their Subelements

Chorus riser element					Subelement			
No.	Date and time	MLT	L	MLAT ($^{\circ}$)	No.	Frequency (Hz)	Wave amplitude (nT)	\mathbf{k} direction angle ($^{\circ}$)
1	30 Aug 2014, 02:11 UT	5.8	5.8	3.1	1	900.7 ± 35.1 (3.9%)	± 0.6 to ± 1.1	1.1
					2	1029.0 ± 25.2 (2.4%)	± 0.6 to ± 1.2	9.5
2	3 Sep 2014, 23:06 UT	5.8	5.7	-1.3	3	704.5 ± 10.5 (1.4%)	± 0.1 to ± 0.2	26.7
					4	818.2 ± 17.5 (2.1%)	± 0.16 to ± 0.23	17.0
3	12 May 2014, 10:30 UT	8.9	5.8	8.1	5	1037.5 ± 22.0 (2.1%)	± 0.3 to ± 0.6	16.9
					6	1123.7 ± 27.5 (2.4%)	± 0.3 to ± 0.5	7.4

the chorus elements. Column 6 is the subelement numbers (Subelements 1 and 2 are part of Riser 1, etc.). Column 7 gives the mean frequency of the seven wave cycles of the subelement. In parentheses are the one standard deviation values. Column 8 is the peak wave amplitude in the subelement. Column 9 is the wave direction of propagation relative to the ambient magnetic field direction.

Details of chorus riser Elements 1 and 2 (and Subelements 1 and 2 and 3 and 4, respectively) were given previously. They are repeated here for intercomparison to the other events. Details of chorus riser Element 3 (and Subelements 5 and 6) are given in the supporting information.

4. Summary

The three low-frequency ($f < 0.5$ fce) chorus riser element events selected for analyses were intense, isolated events, occurring within $\pm 10^\circ$ (-1.3° to 8.1°) of the magnetic equator, the wave generation region. The riser events occurred in the inner parts of outer magnetosphere ($L = 5.7$ to 5.8), distances far away from the magnetopause. The local time of the events was from dawn (MLT = 5.8) to local morning (MLT = 8.9). These were “typical” intense chorus events (low-frequency, dayside risers).

From each of the three chorus elements, two subelements were selected for more detailed study. These were selected for their large amplitudes. The subelements within each element were selected so that they were not adjacent to each other but separated by one or more other subelements. The selected subelements were numbered from 1 to 6 and were shown in detail in Figures 3, 4, 7, 8, A3, and A4, respectively. To examine the constancy in frequency of the subelements, minimum variance analyses (Sonnerup & Cahill, 1967) were performed for each subelement and the zero crossings of the B1 component (maximum variance direction) were used to identify the start and stop times of each wave cycle. The cycle duration was converted to a “frequency” so that the frequencies of the cycles could be intercompared. A continuous wavelet power spectrum was also created for the subelement intervals.

Our study has found that:

1. The frequencies were most constant where the wave amplitudes within the subelement were the most intense (the central portions of the subelements analyzed).
2. All of the chorus subelements exhibited essentially the same features. There were no obvious continuous frequency upward ramping throughout any of the six subelements analyzed. The frequencies of the wave cycles were constant within 2.1% to 3.9% of the mean value (\pm one standard deviation).
3. The greatest frequency deviations within a subelement occurred near the edges where the wave amplitudes were either increasing or decreasing, leading to the start or end of the “packets.” Both increase and decrease of frequency were noted at both ends of the packets.

One referee has requested that we expand our comments in the Summary and Item 3 in specific. In looking at both the beginning and end of each of the six subelements, we find for Subelement 1 rising and rising, Subelement 2 rising and falling, Subelement 3 falling and falling, Subelement 4 rising and rising, Subelement 5 constant and constant, and Subelement 6 rising and falling. For a constant upward sweep in a chorus element, one would expect that rising frequency should occur at both ends of the subelement. What we find from the six subelements are six risings, four fallings, and two constant. Based on this and Item 1 above, we have concluded that our results imply Item 2, that “there were no obvious continuous frequency upward ramping”.

Theory (Nunn, 1986; Omura et al., 2008; Trakhengerts et al., 2004) and observations (Cully et al., 2011) have found sweep rates of 3–10 kHz/s on average corresponding to a 20–50 Hz rise over a seven cycle period. The referee has pointed out that Subelements 1, 2, and 4 show frequency increases of 20–30 Hz over their full seven cycle duration. However, one should point out that Subelements 3 and 6 did not show such frequency rises.

There is a clear and fast frequency decrease of ~ 50 Hz with Subelement 6. The referee points out that with our standard deviation of 3% implying uncertainty of ~ 30 Hz, one cannot say for certainty that this is inconsistent with nonlinear theory of Omura et al. (2008) and Trakhengerts et al. (2004). We agree with the referee. In doing this analyses we are up against the uncertainty principle and cannot delve further in frequency resolution. However, in all fairness we have to say that this same argument holds for the

discussion for all subelements as well. All we can say is by examining these six subelements, the conclusion that we can gather is that they are on average monochromatic.

The referee also points out that the theoretical frequency sweep rate can become smaller with smaller wave amplitudes. This may possibly explain the constant frequency of Subelement 3.

4.1. Final Comments and Conclusions

The approximate monochromaticity of the wave frequencies within the chorus subelements is somewhat different than the smoothly increasing frequency variations obtained from simulation works by Omura et al. (2008), Omura (private communication, 2019), and Lu et al. (2019). The constancy of wave frequency in the center of the wave packets/subelements where the wave amplitudes were largest was different than that expected by sideband emission generation (Nunn, 1986; Trakhengerts et al., 2004). However, one should add if one considers the uncertainty of frequency determination, the results presented here are not inconsistent with the models of nonlinear chorus generation presented by Nunn (1986), Nunn et al. (2005), and Omura and Nunn (2011). Their simulation results often show a near-constant frequency inside subelements.

Nunn et al. (2005) have provided an explanation for rising tones with upper sideband instability allowing successive jumps to the next upper sideband through the establishment of a spatial frequency gradient by the out-of-phase portion of the resonant current. Hanzelka et al. (2020) have derived a new model for the formation of subelements. The latter authors assume that the resonant current is released and propagates upstream to generate a new whistler wave with increased frequency. This wave then triggers a new subelement.

This leaves a fundamental question of how and why chorus elements are structured the way they are. We think that some modifications of nonlinear theories will be needed to explain the approximately monochromatic chorus subelement structure.

The approximate monochromaticity of each of the subelements indicates that the subelement waves are most likely generated by a narrow energy range of energetic electrons. Phase bunching of the electrons would be one way of generating the coherent waves. Each higher-frequency subelement in a chorus riser element would involve a lower energy range of cyclotron resonant energetic electrons. Thus, the sweeping of the chorus riser could first involve instability of ~40 keV electrons at the beginning and then ~6 keV electrons at the end, giving the general structure of the rising frequency chorus element. A revised model will have to explain why the phase bunching of the ~40 keV electrons occurs first and the ~6 keV electrons last. Another, related difficulty is how each subelement stimulates the next one at a slightly higher frequency, and so on. This latter issue has been addressed by several models referred to earlier.

The referee has asked us to mention that “Artemyev et al. (2015), Kubota and Omura (2018), Mourenas et al. (2018), and Tao et al. (2013) have shown that the efficiency of nonlinear electron interaction with coherent chorus can be strongly altered.” As shown in this paper if one simply assumes the cyclotron resonance condition, the first, lowest frequency subelement in a chorus riser will scatter ~40 keV electrons and then lower and lower energies. Now, with the establishment that chorus subelements are nearly monochromatic, the electron energy bands being scattered will be even tighter. The effect of these interactions should be observed in the ionosphere as energy dispersion of the arriving electrons. A seminal rocket experiment performed by Lampton (1967) studying microbursts did not find the expected electron dispersion. Thus, further studies on this topic are needed.

One fundamental difficulty of chorus generation that theories have not addressed yet is if one has an extensive cloud of energetic electrons drifting from midnight through dawn to local noon (see Tsurutani & Smith, 1977), why is chorus observed to be generated for hours? Where is all the free energy for chorus coming from? Why are there overlapping rising tones as shown here in this paper and elsewhere? One thought is that free energy must be continuously being pumped into the electron cloud. One possibility is to have energy dispersion created by the gradient drift of the energetic electrons supply the free energy. In the day-side magnetosphere where the solar wind has compressed the magnetic fields, drift shell splitting will take place allowing a further separation of more energetic electrons from those of lesser energies. These two factors may be able to provide the free energy needed.

Appendix A: An Additional Chorus Element Examination

We examine one more intense chorus riser interval. The same format for Figures 1 to 4 are used here.

We show a different type of a chorus riser element in Figure A1. These, like the previous two elements of Figures 1 and 5, were selected with the criteria indicated in section 2. This chorus event occurred on 12 May 2014 at ~10:30 UT. The event occurred at a $L = 5.8$, the inner part of the outer radiation belt, at a MLT of 8.9 in local morning and at a MLAT of 8.1° . The waves were propagating at an angle $\sim 16.2^\circ$ relative to \mathbf{B}_0 .

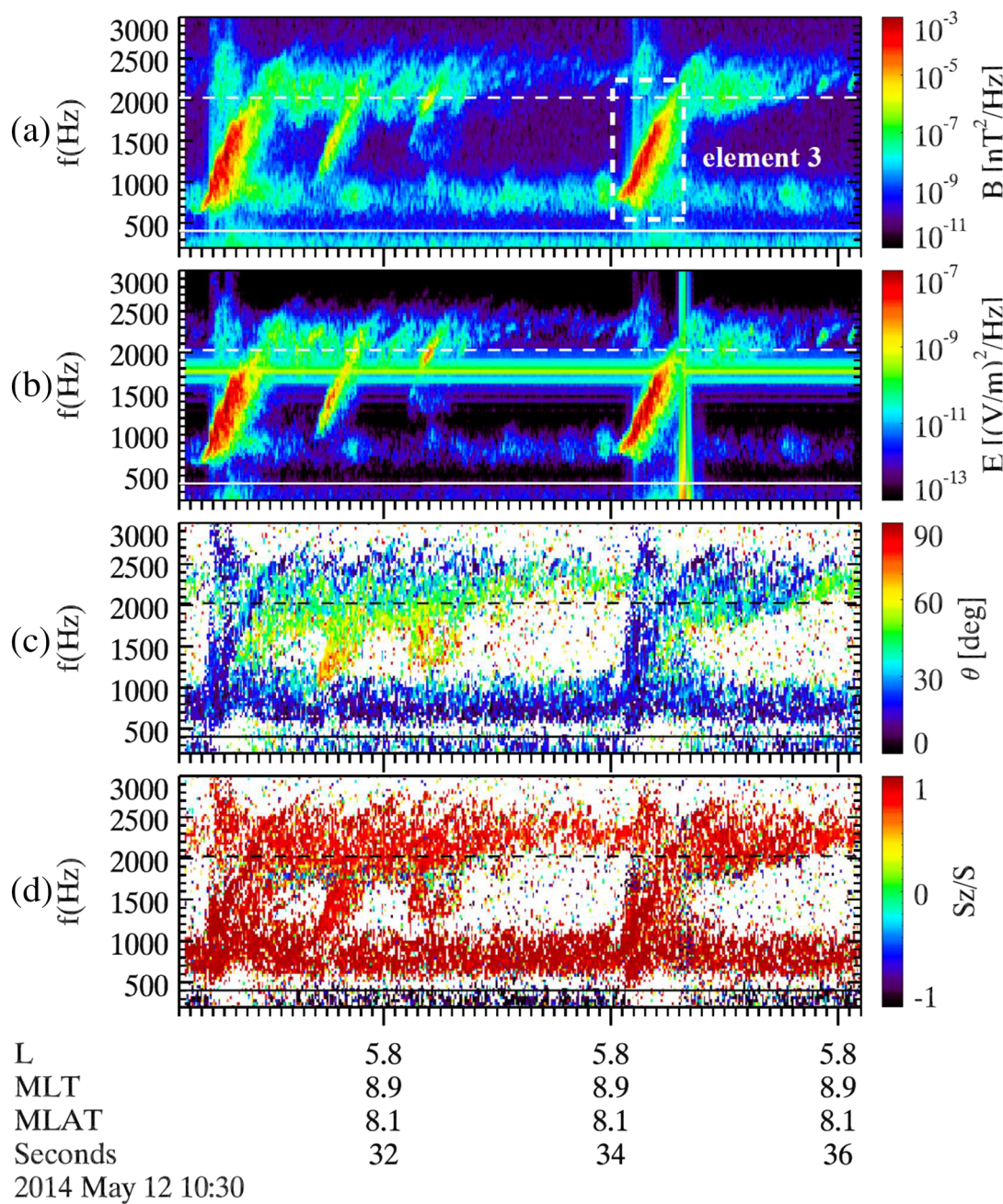


Figure A1. Several chorus rising elements taken on 12 May 2014 at ~10:30 UT. The format is the same as in Figure 1 in the main body of the text. Chorus riser Element 3 is indicated by a white dashed box.

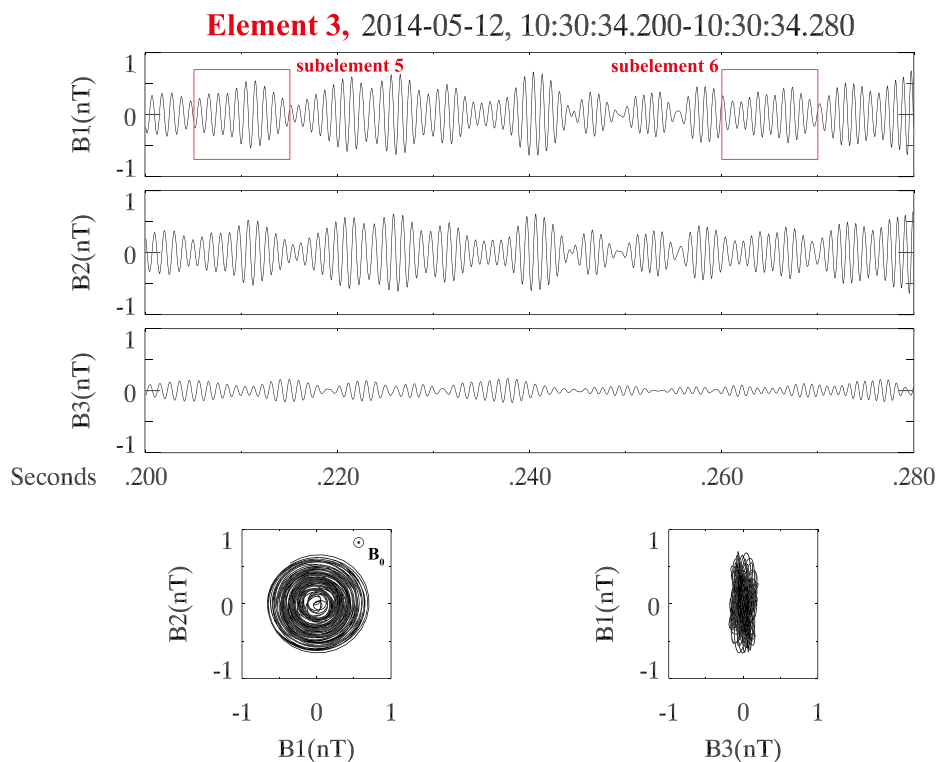


Figure A2. A high-resolution display of Element 3 taken at ~1030:34 UT 12 May 2014. The format is the same as in Figure 2.

The chorus riser elements started near a low-frequency portion of a hiss band at ~650 Hz and rose to ~2500 Hz or from ~0.2 to ~0.6 fce. What is different about this particular event is that the chorus elements sometimes crossed the ~0.5 fce “gap.” It is noted that the amplitude of the two most intense elements at ~1032:30 and 1032:34 UT showed a reduction in intensity as the riser approached ~0.45 fce. The wave intensity was diminished from ~0.45 to 0.6 fce. At ~1032:32 UT there are three less intense riser elements which maintain their low intensities from ~1800 to ~2300 Hz across the ~0.5 fce gap. The hypothesis of Landau damping causing the ~0.5 fce gap might be the correct mechanism (Omura et al., 2009; Taubenschuss et al., 2015; Tsurutani & Smith, 1974). However, Li, Thorne, et al. (2011) and Li et al. (2016) have indicated that the upper band of chorus might have a different source of generation. Thus, only the lower frequency band ($f < 0.5$ fce) portion of the chorus riser has been selected for study.

Panels (c) and (d) indicate that the waves are traveling parallel to \mathbf{B}_0 . The quantity $Sz/S \sim 1.0$.

The isolated riser at ~1032:34 UT was selected for detailed analyses. A white dashed box surrounds the riser in panel (a). This is Element 3.

Figure A2 shows that chorus riser Element 3 is composed of many subelements. In this 0.08 s display there are 12 distinct subelements. Each subelement has only approximately three to five or six wave cycles at the highest amplitudes. None of the subelements have steady constant amplitudes like those displayed in Elements 1 and 2. The waves in Figure A2 are right-hand circularly polarized and planar. The waves are propagating at ~8.3° relative to \mathbf{B}_0 . Two intervals have been selected for further analyses indicated by the red boxes in the top panel. These are Subelements 5 and 6.

Figure A3 shows that Subelement 5 is right-hand circularly polarized. The waves are propagating at ~16.9° relative to the ambient magnetic field \mathbf{B}_0 and are plane polarized.

The wave amplitude shown in the figure starts with two cycles of amplitude $\sim\pm0.3$ nT and frequency of 1024 Hz. In Cycles 3 and 4, the amplitude increases to $\sim\pm0.5$ nT by Cycles 4 and 5 as the frequency rises

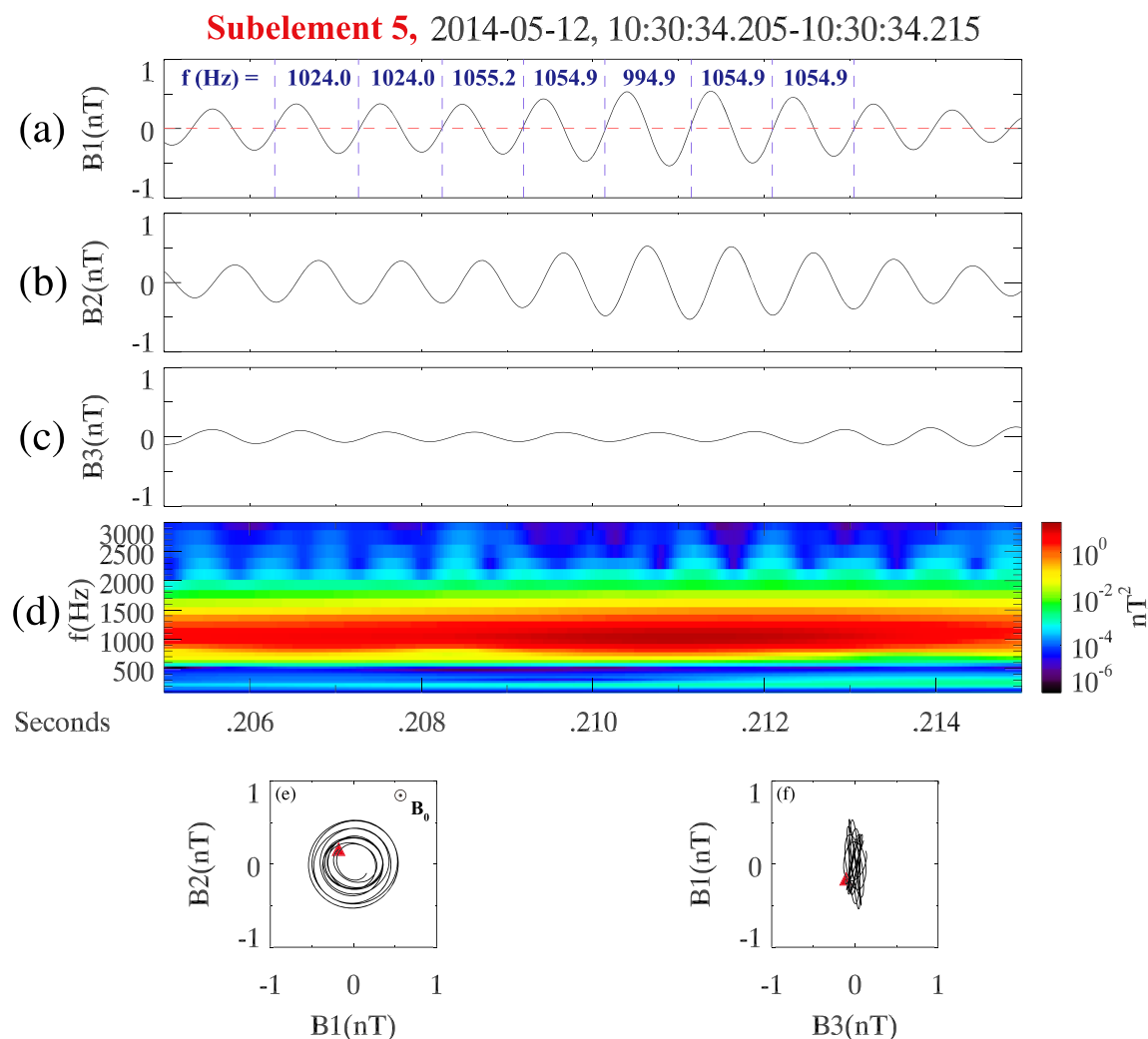


Figure A3. (a-d) Subelement 5 shown in high resolution. This is part of Element 3 identified in Figures A1 and A2.

to 1055 Hz. Cycle 5 contains the peak packet amplitude of $\sim \pm 0.6$ nT. Cycle 5 has the minimum frequency of 995 Hz. As the waves in the packet decrease in amplitude (Cycles 6 and 7), the frequency increases back to 1024 Hz. Cycle 7 has an amplitude of $\sim \pm 0.4$ nT. There is no obvious frequency trend seen in these results. The wavelet power spectrogram shows the same feature of no obvious frequency trend with time.

The mean frequency for the seven cycles is 1037.5 Hz with a standard deviation of 22.0 Hz. This standard deviation is 2.1% of the mean frequency.

Subelement 6 is shown in Figure A4. Again, the waves are right-hand polarized and planar, as expected. The waves are propagating at $\sim 7.4^\circ$ relative to \mathbf{B}_0 . Seven wave cycles have been analyzed for their frequencies. Here it is noted that the first cycle starts at 1123 Hz with an amplitude of $\sim \pm 0.3$ nT. Cycles 3 and 4 have the same frequency at a slightly higher amplitude of $\sim \pm 0.4$ nT. Cycles 6 and 7 have the highest amplitudes of ± 0.5 nT with a frequency of 1087.7 Hz. Thus, in this case the frequency seemed to decrease with time even though the amplitude increased. There is no obvious strong frequency trend with time.

The wavelet power spectral peak shows a slight decrease in frequency across the subelement. This is consistent with the single cycle wave analyses.

The mean frequency for the seven cycles of Subelement 6 was 1123.7 Hz with a standard deviation of 27.5 Hz. This standard deviation is 2.4% of the mean frequency.

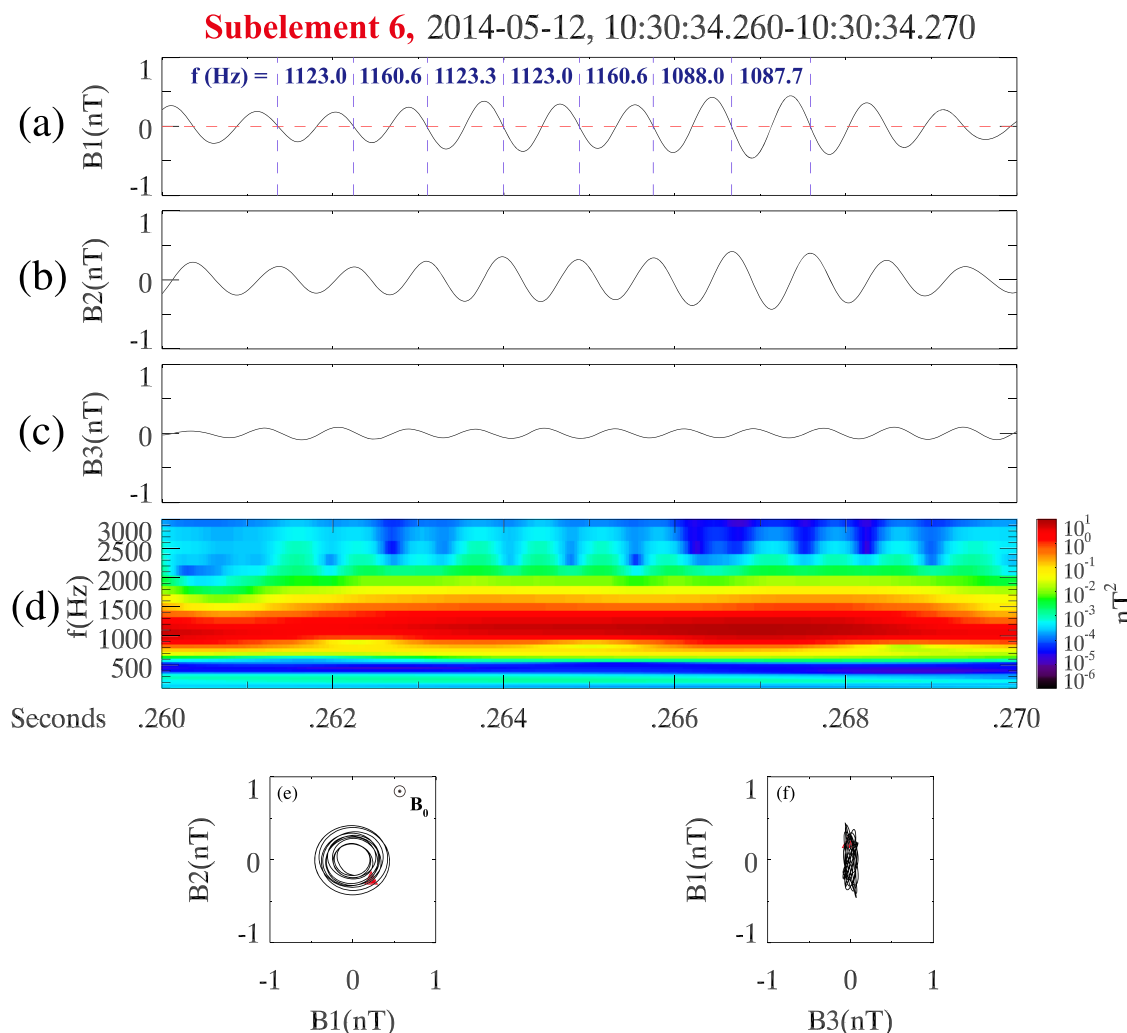


Figure A4. (a–d) Subelement 6, part of Element 3 shown in Figures A1 and A2.

Acknowledgments

X. G. acknowledges the support of NSFC Grant 4177415. The work done by Q. L. was supported by the NSFC Grants 41527804 and 41774169 and the Key Research Program of Frontier Sciences, CAS (QYZDJ-SSW-DQC010). G. S. L is thankful to the Indian National Science Academy for the support under the INSA-Honorary Scientist Scheme. A. S. is thankful to the Indian National Science Academy (INSA) for the support under the INSA Senior Scientist Fellowship scheme. The work by R. H. was funded by the Science & Technology Research Board (SERB), a statutory body of the Department of Science and Technology (DST), India, through the Ramanujan Fellowship. Portions of the research were performed at the Jet Propulsion Laboratory, California Institute of Technology under contract with NASA.

The mean frequency for Subelement 6 was 1123.7 Hz compared to the mean frequency for Subelement 5 of 1037.5 Hz. The higher frequency of Subelement 6 is expected for a rising tone element since Subelement 6 occurred later in time.

Data Availability Statement

The Van Allen Probes plasma wave and magnetic field data can be obtained from the <https://spdf.gsfc.nasa.gov/pub/data/rbsp/> website. Portions of this research was carried out at the Jet Propulsion Laboratory, California Institute of Technology under contract with NASA.

References

- Agapitov, O., Artemyev, A., Krasnoselskikh, V., Khotyaintsev, Y. V., Mourenas, D., Breuillard, H., et al. (2013). Statistics of whistler mode waves in the outer radiation belt: Cluster STAFF-SA measurements. *Journal of Geophysical Research: Space Physics*, 118, 3407–3420. <https://doi.org/10.1002/jgra.50312>
- Akasofu, S.-I. (1964). The development of the auroral substorm. *Planetary Space Physics*, 12(4), 273–282. [https://doi.org/10.1016/0032-0633\(64\)90151-5](https://doi.org/10.1016/0032-0633(64)90151-5)
- Anderson, K. A., & Milton, D. W. (1964). Balloon observation of X-rays in the auroral zone III, high time resolution studies. *Journal of Geophysical Research*, 69(21), 4457–4479. <https://doi.org/10.1029/JZ069i021p04457>
- Artemyev, A. V., Mourenas, D., Agapitov, O. V., Vainchtein, D. L., & Mozer, F. S. (2015). Stability of relativistic electron trapping by strong whistler or electromagnetic ion cyclotron waves. *Physics of Plasmas*, 22, 082901. <https://doi.org/10.1063/1/4927774>

- Aryan, H., Yearby, K., Balikhin, M., Agapitov, O., Krasnoselskikh, V., & Boynton, R. (2014). Statistical study of chorus wave distributions in the inner magnetosphere using Ae and solar wind parameters. *Journal of Geophysical Research: Space Physics*, 119, 6131–6144. <https://doi.org/10.1002/2014JA019939>
- Bellan, P. M. (2013). Pitch angle scattering of an energetic magnetized particle by a circularly polarized electromagnetic wave. *Physics of Plasmas*, 20, 042117. <https://doi.org/10.1063/1.4801055>
- Breuillard, H., Agapitov, O., Artemyev, A., Krasnoselski, V., Le Contel, O., Cully, C. M., et al. (2014). On the origin of falling-tone chorus elements in Earth's inner magnetosphere. *Annales de Géophysique*, 32(12), 1477–1485. <https://doi.org/10.5194/ageo-32-1477-2014>
- Compernolle, B. V., An, X., Bortnik, J., Thorne, R. M., Pribyl, P., & Gekelman, W. (2015). Excitation of chirping whistler waves in a laboratory plasma. *Physical Review Letters*, 114, 245002. <https://doi.org/10.1103/PhysRevLett.114.245002>
- Cully, C. M., Angelopoulos, V., Auster, U., Bortnik, J., Bonnell, J., & Le Contel, O. (2011). Observational evidence of the generation mechanism for rising-tone chorus. *Geophysical Research Letters*, 38, L01106. <https://doi.org/10.1029/2010GL045793>
- DeForest, S. E., & McIlwain, C. E. (1971). Plasma clouds in the magnetosphere. *Journal of Geophysical Research*, 76(16), 3587–3611. <https://doi.org/10.1029/JA076i016p03587>
- Demekhov, A. G., Taubenschuss, U., & Santolik, O. (2017). Simulation of VLF chorus emissions in the magnetosphere and comparison with THEMIS spacecraft data. *Journal of Geophysical Research: Space Physics*, 122, 166–184. <https://doi.org/10.1002/2016JA023057>
- Dungey, J. W. (1961). Interplanetary magnetic field and the auroral zones. *Physical Review Letters*, 6(2), 47–48. <https://doi.org/10.1103/PhysRevLett.6.47>
- Goldstein, B. E., & Tsurutani, B. T. (1984). Wave normal directions of chorus near the equatorial source region. *Journal of Geophysical Research*, 89(A5), 2789–2810. <https://doi.org/10.1029/JA089iA05p02789>
- Hanzelka, M., Santolik, O., Omura, Y., Kolmasova, I., & Kletzing, C. A. (2020). A model of the subpacket structure of rising tone chorus emissions, to appear. *Journal of Geophysical Research: Space Physics*, 125, e2020JA028094. <https://doi.org/10.1029/2020JA028094>
- Heidbrink, W. W. (1995). Beam-driven chirping instability in DIII-D. *Plasma Physics and Controlled Fusion*, 37(9), 937–949. <https://doi.org/10.1088/0741-3335/37/9/002>
- Helliwell, R. A. (1965). *Whistlers and related ionospheric phenomena*. Stanford, California: Stanford University Press.
- Isted, G. A., & Millington, G. (1957). The “dawn chorus” in radio observations. *Nature*, 180(4588), 716. <https://doi.org/10.1038/180716a0>
- Kennel, C. F., & Petschek, H. E. (1966). Limit on stably trapped particle fluxes. *Journal of Geophysical Research*, 71(1), 1–28. <https://doi.org/10.1029/JZ071i001p00001>
- Kletzing, C. A., Kurth, W. S., Acuna, M., MacDowall, R. J., Torbert, R. B., Averkamp, T., et al. (2013). The electric and magnetic field instrument suite and integrated science (EMFISIS) on RBSP. *Space Science Reviews*, 179(1–4), 127–181. <https://doi.org/10.1007/s11214-013-9993-6>
- Kubota, Y., & Omura, Y. (2018). Nonlinear dynamics of radiation belt electrons interacting with chorus emissions localized in longitude. *Journal of Geophysical Research: Space Physics*, 123, 4835–4857. <https://doi.org/10.1029/2017JA02505>
- Lakhina, G. S., Tsurutani, B. T., Verkhoglyadova, O. P., & Pickett, J. S. (2010). Pitch angle transport of electrons due to cyclotron interactions with coherent chorus subelements. *Journal of Geophysical Research*, 117, A00F15. <https://doi.org/10.1029/2009JA014885>
- Lampton, M. (1967). Daytime observations of energetic auroral-zone electrons. *Journal of Geophysical Research*, 72(23), 5817–5823. <https://doi.org/10.1029/JZ072i023p05817>
- Lauben, D. S., Inan, U. S., Bell, T. F., & Gurnett, D. A. (2002). Source characteristics of ELF/VLF chorus. *Journal of Geophysical Research*, 107, 1429. <https://doi.org/10.1029/2000JA003019>
- LeDocq, M. J., Gurnett, D. A., & Hospodarsky, G. B. (1998). Chorus source locations from VLF Poynting flux measurements with the Polar spacecraft. *Geophysical Research Letters*, 25(21), 4063–4066. <https://doi.org/10.1029/1998GL900071>
- Li, W., Bortnik, J., Thorne, R. M., & Angelopoulos, V. (2011). Global distribution of wave amplitudes and wave normal angles of chorus waves using THEMIS wave observations. *Journal of Geophysical Research*, 116, A12205. <https://doi.org/10.1029/2011JA017035>
- Li, W., Santolik, O., Bortnik, J., Thorne, R. M., Kletzing, C. A., Kurth, W. S., & Hospodarsky, G. B. (2016). New chorus wave properties near the equator from Van Allen Probes wave observations. *Geophysical Research Letters*, 43, 4725–4735. <https://doi.org/10.1002/2016GL068780>
- Li, W., Thorne, R. M., Bortnik, J., Shprits, Y. Y., Nishimura, Y., Angelopoulos, V., et al. (2011). Typical properties of rising and falling tone chorus waves. *Geophysical Research Letters*, 38, L14103. <https://doi.org/10.1029/2011GL047925>
- Lu, Q. M., Ke, Y., Wang, X., Liu, K., Gao, X., Chen, L., & Wang, S. (2019). Two-dimension gcPIC simulation of rising-tone chorus waves in a dipole magnetic field. *Journal of Geophysical Research: Space Physics*, 124, 4157–4167. <https://doi.org/10.1029/2019JA026586>
- McGuire, K., Goldston, R., Bell, M., Bitter, M., Bol, K., Brau, K., et al. (1983). Study of high-beta magnetohydrodynamic modes and fast-ion losses in PDX. *Physical Review Letters*, 50(12), 891–895. <https://doi.org/10.1103/PhysRevLett.50.891>
- Meredith, N. P., Cain, M., Horne, R. B., Thorne, R. M., Summers, D., & Anderson, R. R. (2003). Evidence for chorus-driven electron acceleration to relativistic energies from a survey of geomagnetically disturbed periods. *Journal of Geophysical Research*, 108, 1248. <https://doi.org/10.1029/2002JA009764>
- Meredith, N. P., Horne, R. B., & Anderson, R. R. (2001). Substorm dependence of chorus amplitudes: Implications for the acceleration of electrons to relativistic energies. *Journal of Geophysical Research*, 106(A7), 13,165–13,178. <https://doi.org/10.1029/2000JA900156>
- Mourenas, D., Zhang, X.-J., Artemyev, A. V., Angelopoulos, V., Thorne, R. M., Bortnik, J., et al. (2018). Electron nonlinear resonant interaction with short and intense parallel chorus wave packets. *Journal of Geophysical Research: Space Physics*, 123, 4979–4999. <https://doi.org/10.1029/2018JA025417>
- Nave, M. F. F., Campbell, D. J., Joffrin, E., Marcus, F. B., Sadler, G., Smeulders, P., & Thomsen, K. (1991). Fishbone activity in JET. *Nuclear Fusion*, 31(4), 697–710. <https://doi.org/10.1088/0029-5515/31/4/007>
- Nunn, D. (1986). A nonlinear theory of sideband stability in ducted whistler mode waves. *Planetary and Space Science*, 34(5), 429–451. [https://doi.org/10.1016/0032-0633\(86\)90032-2](https://doi.org/10.1016/0032-0633(86)90032-2)
- Nunn, D., Rycroft, M., & Trakhtengerts, V. (2005). A parametric study of the numerical simulations of triggered emissions. *Annales de Géophysique*, 33, 3655–3666.
- Omura, Y., Hikishima, M., Katoh, Y., Summers, D., & Yagitani, S. (2009). Nonlinear mechanisms of lower-band and upper-band VLF chorus emissions in the magnetosphere. *Journal of Geophysical Research*, 114, A07217. <https://doi.org/10.1029/2009JA014206>
- Omura, Y., Katoh, Y., & Summers, D. (2008). Theory and simulation of the generation of whistler mode chorus. *Journal of Geophysical Research*, 113, A04233. <https://doi.org/10.1029/2007JA012622>
- Omura, Y., & Nunn, D. (2011). Triggering process of whistler mode chorus emissions in the magnetosphere. *Journal of Geophysical Research*, 116, A05205. <https://doi.org/10.1029/2010JA016280>

- Santolik, O., Gurnett, D. A., Pickett, J. S., Parrot, M., & Cornilleau-Wehrlin, N. (2003). Spatio-temporal structure of storm-time chorus. *Journal of Geophysical Research*, 108, 1278. <https://doi.org/10.1029/2002JA009791>
- Santolik, O., Gurnett, D. A., Pickett, J. S., Parrot, M., & Cornilleau-Wehrlin, N. (2004). A microscopic and nanoscopic view of storm-time chorus on 31 March 2001. *Geophysical Research Letters*, 31, L02801. <https://doi.org/10.1029/2003GL018757>
- Schriger, D., Ashour-Abdalla, M., Coroniti, F. V., LeBoeuf, J. N., Decyk, V., Travnick, P., et al. (2010). Generation of whistler mode emissions in the inner magnetosphere: An event study. *Journal of Geophysical Research*, 115, A00F17. <https://doi.org/10.1029/2009JA014932>
- Smith, E. J., & Tsurutani, B. T. (1976). Magnetosheath lion roars. *Journal of Geophysical Research*, 81(13), 2261–2266. <https://doi.org/10.1029/JA081i013p02261>
- Sonnerup, B. U., & Cahill, L. J. Jr. (1967). Magnetopause structure and attitude from Explorer 12 observations. *Journal of Geophysical Research*, 72(1), 171–183. <https://doi.org/10.1029/JZ072i001p00171>
- Soraas, F., Aarsnes, K., Oksavik, K., Sandanger, M. I., Evans, D. S., & Greer, M. S. (2004). Evidence for particle injection as the case of Dst reduction during HILDCAA events. *Journal of Atmospheric and Solar - Terrestrial Physics*, 66(2), 177–186. <https://doi.org/10.1016/j.jastp.2003.05.001>
- Storey, L. R. O. (1953). An investigation of whistling atmospherics. *Philosophical Transactions of the Royal Society B*, 246, 113–141.
- Tao, X., Bortnik, J., Albert, J. M., Thorne, R. M., & Li, W. (2013). The importance of amplitude modulation in nonlinear interactions between electrons and large amplitude whistler waves. *Journal of Atmospheric and Solar - Terrestrial Physics*, 99, 67–72. <https://doi.org/10.1016/j.jastp.2012.05.012>
- Taubenschuss, U., Khotyaintsev, Y. V., Santolik, O., Vaivads, A., Cully, C. M., Le Contel, O., & Angelopoulos, V. (2014). Wave normal angles of whistler mode chorus rising and falling tones. *Journal of Geophysical Research: Space Physics*, 119, 9567–9578. <https://doi.org/10.1002/2014JA020575>
- Taubenschuss, U., Santolik, O., Breuillard, H., Li, W., & Le Contel, O. (2016). Poynting vector and wave vector directions of equatorial chorus. *Journal of Geophysical Research: Space Physics*, 121, 11,912–11,928. <https://doi.org/10.1002/2016JA023389>
- Taubenschuss, U., Santolik, O., Graham, D. B., Fu, H., Khotyaintsev, Y. V., & Le Contel, O. (2015). Different types of whistler mode chorus in the equatorial source region. *Geophysical Research Letters*, 42, 8271–8279. <https://doi.org/10.1002/2015GL066004>
- Trakhengerts, V. Y., Demenkov, A. G., Titova, E. E., Kozetov, B. V., Santolik, O., Gurnett, D., & Parrot, M. (2004). Interpretation of cluster data on chorus emissions using the backward wave oscillator model. *Physics of Plasmas*, 11(4), 1345–1351. <https://doi.org/10.1063/1/1667495>
- Tsurutani, B. T., Falkowski, B. J., Verkhoglyadova, O. P., Pickett, J. S., Santolik, O., & Lakhina, G. S. (2011). Quasi-coherent chorus properties: 1. Implications for wave-particle interactions. *Journal of Geophysical Research*, 116, A09210. <https://doi.org/10.1029/2010JA016237>
- Tsurutani, B. T., Lakhina, G. S., & Hajra, R. (2020). The physics of space weather/solar-terrestrial physics (STP): What we know now and what the current and future challenges are. *Nonlinear Processes in Geophysics*, 27(1), 75–119. <https://doi.org/10.5194/npg-27-75-2020>
- Tsurutani, B. T., Lakhina, G. S., & Verkhoglyadova, O. P. (2013). Energetic electron (>10 keV) microburst precipitation, ~5–15 s X-ray pulsations, chorus and wave-particle interactions: A review. *Journal of Geophysical Research: Space Physics*, 118, 2296–2312. <https://doi.org/10.1002/jgra.50264>
- Tsurutani, B. T., McPherron, R. L., Gonzalez, W. D., Lu, G., Gopalswamy, N., & Guarnieri, F. L. (2006). Magnetic storms caused by corotating solar wind streams. In B. T. Tsurutani, et al. (Eds.), *Recurrent magnetic storms: Corotating solar wind streams* (Vol. 167, pp. 1–17). Washington DC: American Geophysical Union Press. <https://doi.org/10.1029/167GM03>
- Tsurutani, B. T., & Meng, C.-I. (1972). Interplanetary magnetic field variations and substorm activity. *Journal of Geophysical Research*, 77(16), 2964–2970. <https://doi.org/10.1029/JA077i016p02964>
- Tsurutani, B. T., & Smith, E. J. (1974). Postmidnight chorus: A substorm phenomenon. *Journal of Geophysical Research*, 79(1), 118–127. <https://doi.org/10.1029/JA079i001p00118>
- Tsurutani, B. T., & Smith, E. J. (1977). Two types of magnetospheric ELF chorus and their substorm dependences. *Journal of Geophysical Research*, 82(32), 5112–5128. <https://doi.org/10.1029/JA082i032p05112>
- Tsurutani, B. T., Smith, E. J., West, H. I. Jr., & Buck, R. M. (1979). Chorus, energetic electrons and magnetospheric substorms. In P. J. Palmadesso & K. Papadopoulos (Eds.), *Wave instabilities in space plasmas* (Vol. 55–71, pp. 55–62). Amsterdam: D. Reidel.
- Tsurutani, B. T., Verkhoglyadova, O. P., Lakhina, G. S., & Yagitani, S. (2009). Properties of dayside outer zone chorus during HILDCAA events: Loss of energetic electrons. *Journal of Geophysical Research*, 114, A03207. <https://doi.org/10.1029/2008JA013353>
- Verkhoglyadova, O. P., Tsurutani, B. T., & Lakhina, G. S. (2010). Properties of obliquely propagating chorus. *Journal of Geophysical Research*, 115, A00F19. <https://doi.org/10.1029/2009JA014809>
- Yoon, D. Y., & Bellan, P. M. (2020). Non-diffusive pitch-angle scattering of a distribution of energetic particles by coherent whistler waves. *Journal of Geophysical Research: Space Physics*, 125, e2020JA027796. <https://doi.org/10.1029/2020JA027796>